


Tunable Locally Resonant Surface-Acoustic-Waveguiding Behavior by Acoustoelectric Interaction in ZnO-Based Phononic Crystal

F. Taleb and S. Darbari*

Nano Sensors and Detectors Lab., and Nano Plasmophotonic Research Group, Faculty of Electrical and Computer Engineering, Tarbiat Modares University, Tehran 1411713116, Iran

 (Received 25 July 2018; revised manuscript received 28 November 2018; published 12 February 2019)

We present a phononic crystal based on ZnO pillars on a Si substrate that creates local-resonance band gaps, prohibiting surface-acoustic-wave propagation. The created local-resonance band gaps originate from Fano-resonance between the pillars and the substrate, and are shown to be highly influenced by the structural parameters of the pillars. Regarding surface acoustic waveguiding, we introduce a line defect to the crystal where elastic energy can be confined, leading to defect modes with slow group velocity. It is shown that the emerged defect guiding modes can be conducted into the local-resonance gap by adjusting the structural parameters of the defects. Moreover, it is proven that hollow cylinders in the linear defect introduce higher degrees of freedom in the structural parameters of the defect for adjusting the guiding mode, and can lead to narrow-band guiding modes in comparison with the gap width at the vicinity of the mid gap. The achieved narrow-band guiding modes are attributed to the reduced number of allowed resonance frequencies in hollow cylinders due to their reduced effective radius and inherent spatial confinement. Additionally, benefiting from acoustoelectric interaction in piezoelectric materials, we can modulate the elasticity of the ZnO structures by varying their conductivity, which can lead to efficient tuning of the designed guiding modes. The required conductivity modulation in the ZnO structures is proposed to be achieved by UV illumination so that the photogenerated excess carriers screen the electric field associated with the elastic wave, perturbing the wave propagation and affecting the defect guiding modes. The proposed system opens up perspectives for designing reconfigurable, high-quality-factor surface-acoustic-wave devices such as filters and duplexers. The achieved maximum shift of the guiding frequency is about 100 MHz for a defect frequency of 4.18 GHz and a bandwidth of about 100 MHz, suitable for wireless communication applications.

DOI: [10.1103/PhysRevApplied.11.024030](https://doi.org/10.1103/PhysRevApplied.11.024030)

I. INTRODUCTION

Periodic arrays of scatterers with different elastic properties from those of the background media, which can strongly alter the propagation of elastic and acoustic waves, are known as phononic crystals (PNC). PNCs can create stop bands for elastic-acoustic waves in certain frequency ranges depending on the geometric and elastic parameters of the scatterers [1–3]. PNCs have found numerous applications such as acoustic filters, waveguides, isolators, reflectors, resonators, and demultiplexers, as well as sensors and energy-harvesting devices [4–15]. Moreover, recent advances in nanotechnology have led to the realization of nanodimensional PNCs with high-frequency operating ranges that have opened new application fields, including acoustic metamaterials, heat management, and coupled photonic-phononic applications [16–19].

Discovered in 1885 by Lord Rayleigh, surface acoustic waves (SAW) are characterized by their bounded displacement to a certain vicinity on the surface and their low amplitude as compared to their wavelength [20,21]. The SAW devices are commonly used as rf filters, resonators, and duplexers in wireless communication systems such as cell phone networks [22–27], and in a wide range of sensor platforms including gas, temperature, and magnetic field sensors [28–32]. PNCs with finite thicknesses, known as PNC plates or slabs, can be implemented on the delay line of SAW devices to open complete band gaps for guided SAWs inside the slab [33]. Acoustic waves traveling in the PNC slabs can lead to the formation of guided modes, which are confined to the vicinity of the slab surface and the scatterers. The band gaps in PNCs generally result from the destructive interference of scattered waves, which is known as Bragg scattering. The frequency range of this band gap inversely depends on the PNC's lattice constant dimension, thus it is limited by the dimensions of the PNCs. The necessity for the creation of band gaps in frequency ranges, which are not constrained

*s.darbari@modares.ac.ir

by the PNC's unit cell dimension, has attracted major attention to a new type of band gap known as the local resonance-gap. Local-resonance structures, that is, pillars, that can be arrayed to form a PNC and can show Fano-like interference with the substrate, resulting in the appearance of new modes called surface-coupled modes, which are a hybrid of the resonance modes of the resonators and the surface modes of the substrate. In consequence, the local-resonance band gaps accordingly appear in the absence of these modes [34]. There are several publications that report numerical and experimental studies on local-resonance band gaps [35–38]. They demonstrate that the local-resonance band gaps are highly influenced by the structural parameters of the PNCs. Moreover, it is well established that point or linear defects inside a PNC can create defect modes inside the local-resonance band gap that can be used to localize elastic waves inside the defect. The resulting transmission peak of the defect can be further utilized in elastic wave guiding and filtering applications [39–41].

In this work, we report a tunable locally resonance surface-acoustic-waveguiding behavior, benefiting from the acoustoelectric interaction in a ZnO-based PNC. We investigate the effect of structural parameters and the shape of the linear defect on the waveguiding characteristics, including guiding frequency and bandwidth. Our results show an optimized waveguiding behavior when using a linear defect based on hollow cylinders. Additionally, benefiting from the acoustoelectric interaction in piezoelectric materials, we can effectively modulate the elasticity of the ZnO structures by varying their conductivity, which can lead to efficient tuning of the optimized guiding modes. Of the all available piezoelectric media, ZnO has been chosen in this work because of its large piezoelectric-coupling coefficient, strong acoustoelectric interaction, and ease of integration with electronic circuits, as well as its simple and low-cost deposition possibilities over nonpiezo materials such as Si [42]. The presented study can be utilized in realizing reconfigurable SAW devices. In this line of research, there are very recent reports, which utilize completely different approaches, including magnetically tunable SAW devices based on a multiferroic substrate [43] and magnetically controlled nonreciprocal SAWs by magnetoelastic and interfacial Dzyaloshinskii-Moriya interactions [44]. Here, we present an optimized waveguide as a SAW filter and successfully prove the tunable performance of the device by modulating the conductivity of the ZnO layer. The final proposed tunable filter is a band-pass shear-horizontal SAW filter, benefiting from high electromechanical coupling and energy concentration near the metallized surface of shear-horizontal waves. Considering the frequency, bandwidth, and tunability of the designed filter, it can be suitable for wireless communication applications such as duplexers [45].

II. STRUCTURE AND PHYSICAL OPERATING PRINCIPLE

It is well known that the interaction of an incident elastic wave with a PNC depends on the elastic and mechanical parameters of the crystal. On the other hand, tailoring a defect inside the PNC can introduce certain defect frequencies inside the stop band of the PNC. These defect frequencies depend on the shape and structural parameters of the defect, as well as the elastic constants. Thus, the guiding frequencies can be engineered by adjusting the structural or elastic parameters of the defect. Since changing the structural parameters of the defect is not feasible after the fabrication process, finding a way to modify the elastic properties of the PNC is preferred to tune the guiding frequencies. Previous studies have shown that acoustoelectric interaction in semiconductor-piezoelectric materials can induce effective perturbations in elastic constants vs conductivity modulation [46]. This interaction occurs due to screening of the electric field associated with the elastic wave propagation in piezoelectric media by excess carriers, which results in an effective change of the media's elasticity [47–51]. Regarding this, we consider a PNC of intrinsic ZnO pillars with a linear defect to achieve a SAW waveguiding behavior in which the elastic constants can be controlled through the acoustoelectric interaction. Consequently, the characteristics of the designed SAW waveguide can be tuned by modulating the conductivity of the material and can be proposed as a reconfigurable SAW filter.

Figure 1 demonstrates a schematic of the proposed tunable PNC-based waveguide and the relating qualitative transmission spectrum. It can be observed that the input SAW is fed through a line source to the delay line, which consists of intrinsic ZnO pillars over Si as the substrate. The proposed ZnO/Si-based structure benefits from a simple low cost and CMOS-compatible fabrication process, suitable for integration goals. ZnO pillars form a square lattice on the delay line, where a linear defect is included

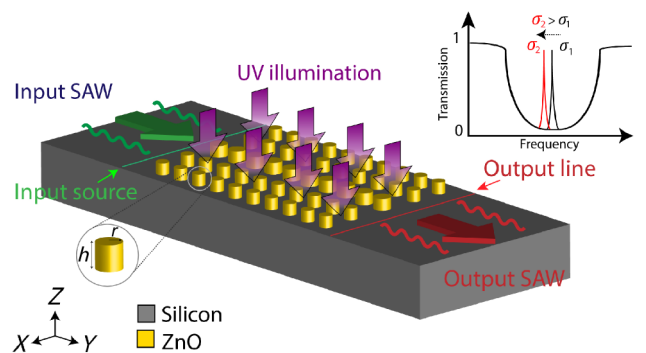


FIG. 1. Schematic of the proposed SAW filter consisting of a ZnO-based PNC. The inset shows the transmission spectra of the filter, corresponding to two different conductivity values $\sigma_1 > \sigma_2$.

to realize the required guiding modes in the forbidden band gap of the PNC. The transmission spectrum of the presented filter is achieved by dividing the average absolute displacement components, collected along the output line probe, as depicted in Fig. 1, by the average absolute displacement components, collected along the input line. Conductivity (σ) modulation of the ZnO pillars leads to tuning the defect frequency of the PNC or the guiding frequency of the filter owing to the acoustoelectric interaction. The needed conductivity modulation can be achieved by contactless UV illumination, as schematically illustrated in Fig. 1. We ignore acoustoelectric interaction in the substrate, due to the centrosymmetric structure of the Si lattice. The inset schematically shows the frequency red shift of the filter's transmission peak because of the increased conductivity.

III. THEORY AND IMPLEMENTATION OF SIMULATION

A. Elastic wave propagation in a linear elastic media

Elastic wave propagation inside an elastic material creates atomic displacements, and thus strain and stress fields in different directions. SAWs are also considered to be a type of elastic wave confined to the surface of the material and its vicinity. Hence, to evaluate SAW propagation in a linear elastic media, such as Si, one should solve coupled Eqs. (1) and (2) [52]:

$$S_{ij} = \frac{1}{2}(\partial_j u_i + \partial_i u_j), \quad i, j = x, y, z, \quad (1)$$

$$T_{ij} = c_{ij} S_{ij}, \quad i, j = x, y, z \quad (2)$$

wherein S , u , T , and c are the strain, the atomic displacement, the stress, and the elastic matrix of the media.

B. Elastic wave propagation in piezoelectric media

Whenever an elastic wave travels through a piezoelectric medium, a strain-induced electric field is generated due to the piezoelectric coupling, as shown in coupled Eqs. (3) and (4) [52]:

$$[T]_{6 \times 1} = [C]_{6 \times 6}[S]_{6 \times 1} - [e]_{6 \times 3}^T [E]_{3 \times 1}, \quad (3)$$

$$[D]_{3 \times 1} = [e]_{3 \times 6}[S]_{6 \times 1} - [\epsilon]_{3 \times 3}[E]_{3 \times 1}, \quad (4)$$

wherein e , ϵ , D , and E are the piezoelectric coupling matrix, dielectric matrix, electric displacement, and electric field, respectively. A set of Eqs. (1)–(4) can be utilized to study the behavior of the presented PNC in response to incident SAWs, and to calculate band structures and transmission spectra. The discussed wave equations are solved numerically by the finite element method in this report.

C. Three-dimensional acoustoelectric formalism in elastic wave propagation for piezoelectric media

In a semiconducting piezoelectric media such as ZnO, whenever excess carriers are added to the material by any means, for example, with illuminating UV, the excess carriers can screen the electric field associated with the traveling elastic wave. This phenomenon can effectively change the elasticity of the piezoelectric material, resulting in variations of the wave's velocity and attenuation. In the low-signal regime, when the excess carrier concentration is well below the number of intrinsic charge carriers, Eq. (5) reveals the relation between the electric displacement and the electric field, wherein σ is the total conductivity of the material [47]:

$$[D]_{3 \times 1} = \frac{-j}{\omega} \sigma [E]_{3 \times 1}. \quad (5)$$

By replacing Eq. (5) by Eq. (4), a new set of equations will be derived for elastic wave propagation in the presence of acoustoelectric interaction. After simplification, Eq. (6) is achieved from simultaneous solution of the obtained set of wave equations, wherein stress will be directly related to the strain by an acoustoelectric-induced effective elastic matrix (C'):

$$[T]_{6 \times 1} = [C']_{6 \times 6}[S]_{6 \times 1}. \quad (6)$$

The C' matrix elements depend on σ , ϵ , frequency (ω), and the piezoelectric parameters of the material. The C' matrix elements for ZnO are described below, where e_{ij} are the piezoelectric coupling matrix elements of ZnO and Y_{ij} are the elements of a matrix defined as in Eq. (8). It can be observed that Y_{ij} depends on σ , ϵ , and ω :

$$[C'] = \begin{bmatrix} c_{11} + e_{31}^2 Y_{33} & c_{12} + e_{31}^2 Y_{33} & c_{13} + e_{31}^2 Y_{33} & 0 & 0 & 0 \\ c_{12} + e_{31}^2 Y_{33} & c_{11} + e_{31}^2 Y_{33} & c_{23} + e_{31} e_{33} Y_{33} & 0 & 0 & 0 \\ c_{13} + e_{31} e_{33} Y_{33} & c_{23} + e_{31} e_{33} Y_{33} & c_{33} + e_{33}^2 Y_{33} & 0 & 0 & 0 \\ 0 & 0 & 0 & c_{44} + e_{15}^2 Y_{22} & 0 & 0 \\ 0 & 0 & 0 & 0 & c_{44} + e_{15}^2 Y_{11} & 0 \\ 0 & 0 & 0 & 0 & 0 & c_{66} \end{bmatrix}, \quad (7)$$

$$[Y] = \begin{bmatrix} \frac{1}{\frac{L}{\omega}\sigma + \epsilon_{11}} & 0 & 0 \\ 0 & \frac{1}{\frac{L}{\omega}\sigma + \epsilon_{22}} & 0 \\ 0 & 0 & \frac{1}{\frac{L}{\omega}\sigma + \epsilon_{33}} \end{bmatrix}. \quad (8)$$

The derived effective elastic matrix as a function of the conductivity is used for the proposed ZnO-based PNC to investigate the acoustoelectric-induced tunability of the filter. A three-dimensional (3D) model and mesh are considered in the finite element method to solve the wave equations and calculate the transmission spectra.

D. Implementation of simulations

Figure 2 shows the investigated geometries used to calculate the dispersion and transmission spectra of the proposed perfect and defective PNCs. Figure 2(a) displays a single unit cell of the perfect PNC where the pillars are parallel to the z axis. The unit cell is considered to be infinite in both the x and y directions in order to calculate the dispersion of the PNC. The lattice constant (a), the height (h), and radius of the pillars (r) are 200, 100, and 65 nm, respectively. The filling factor of the pillars is defined as $f = \pi r^2/a^2$. The thickness of the substrate is chosen to be five times the lattice constant of

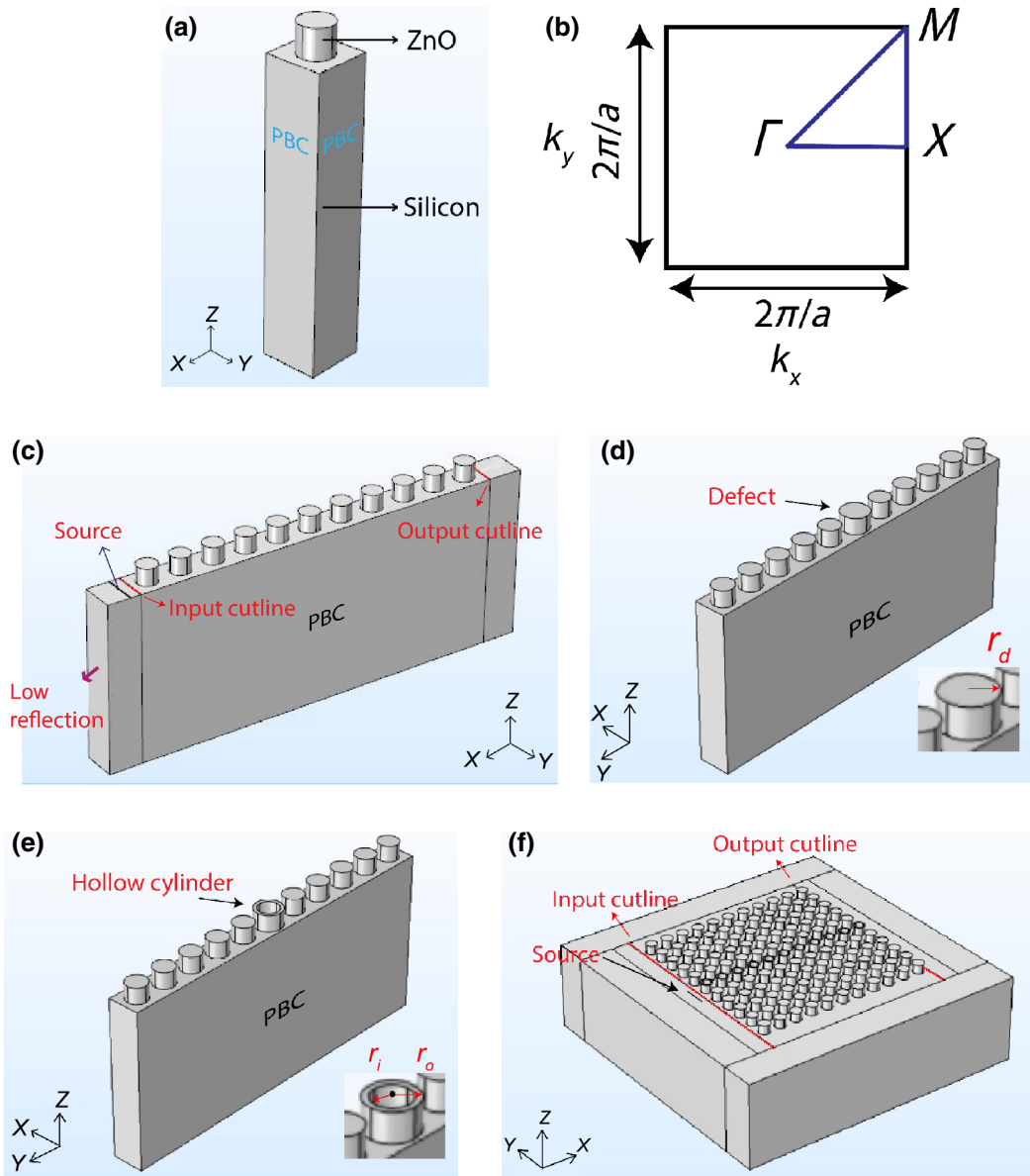


FIG. 2. (a) A unit cell of the PNC and (b) the first Brillouin zone of the crystal. (c) The supercell of the perfect PNC for calculating the transmission spectrum. The supercell of the PNC with: (d) linear pillar defect, and (e) linear hollow cylinder defect, used for band structure calculation. (f) An 11×11 PNC with a linear hollow cylinder defect for calculation of the transmission spectra of the filter.

the unit cell, since the simulation results do not change for larger values of substrate thickness [40]. The substrate material is considered to be Si with elastic constants of $C_{11} = 165.7$ GPa, $C_{12} = 63.9$ GPa, $C_{44} = 79.9$ GPa, and a mass density of $\rho = 2331$ kg/m³. The elastic constants of ZnO as an anisotropic material are considered to be $C_{11} = C_{22} = 209.71$ GPa, $C_{12} = 121.14$ GPa, $C_{13} = 105.39$ GPa, $C_{33} = 211.19$ GPa, $C_{44} = C_{55} = 42.37$ GPa, and $C_{66} = 44.24$ GPa, while the mass density is assumed to be $\rho = 5680$ kg/m³. Bloch-Floquet periodic boundary conditions (PBC) are applied to the lateral sides of the unit cell, and the wave vector in the x and y directions is swept between the high symmetry points of the first Brillouin zone (Γ - X - M - Γ), as shown in Fig. 2(b). A rigid domain boundary condition is applied to the bottom surface of the substrate in order to create surface-coupled modes.

In order to calculate the transmission spectrum for SAW, a supercell with 11 pillars is assumed, which is considered to be finite along the x direction and infinite in the y direction [Fig. 2(c)]. A line source in front of the PNC is utilized to trigger SAWs in the x , y , and z directions and Bloch-Floquet PBCs are applied to the lateral sides of the supercell in the y direction. Layers with high mechanical damping are used around the supercell to minimize the reflections, and low-reflection boundary conditions are applied to the bottom and lateral sides as well to reduce unwanted reflections from the terminating boundaries. We evaluate the transmission spectra of the perfect PNC for the ΓX direction by summing the average absolute values of displacements in the x , y , and z directions over the output cutline and dividing it by the similar average displacement along the input cutline, as highlighted in Fig. 2(c) by red lines. Transmissions for two types of Rayleigh and shear-horizontal waves are calculated accordingly, and the observed band gaps are confirmed by comparing the results with the related calculated band structure.

After investigating the perfect PNC, a line defect consisting of pillars with different radii is added to the structure. Figure 2(d) demonstrates a supercell of 11 pillars with a defect in the middle utilized to calculate the dispersion curve of the PNC. The Bloch-Floquet boundary condition is applied to the lateral sides in the x direction and the wave vector is swept between the Γ and X points of the first Brillouin zone. As the next stage, an alternative defect structure consisting of a line of hollow cylinders is introduced according to Fig. 2(e), which benefits from a higher degree of freedom in structural parameters. For designing narrow-band guiding modes, we use this linear defect in a 11×11 PNC structure and calculate the needed transmission spectra to study the waveguiding transmission peak of the defect inside the band gap [Fig. 2(f)]. A source in front of the PNC creates the desired SAW, while layers with high mechanical damping and low reflection boundaries are used to reduce the reflections from

boundaries. The SAW transmission for the defected PNC is calculated by dividing the sum of the average absolute values of displacement components in the x , y , and z directions collected from the output cutline by the same value collected from the input cutline, as shown by the red lines in Fig. 2(f). It should be noted that in all simulations, we assume intrinsic ZnO for the PNC pillars with negligible conductivity ($\sigma < 0.01$ S/m), except in Fig. 10. However, the conductivity modulation of the ZnO pillars results in tuning the defect frequency of the PNC and the guiding frequency of the filter because of the acoustoelectric interaction. This tuning behavior is achieved because conductivity modulation in piezoelectric semiconductors can induce effective perturbations in elastic constants and the elastic waveguiding. Thus, we have changed σ from 0.001 S/m to 1000 S/m in Fig. 10 to prove the consequent acoustoelectric-induced tunability of the designed SAW filter and confirm the realization of reconfigurable SAW devices.

IV. NUMERICAL RESULTS AND DISCUSSION

A. Perfect PNC

In the very first step, we investigate the effect of the crystal's structural parameters on the behavior of the perfect PNC. It is well established that photonic crystal slabs contain guided modes localized to the slab in addition to radiation states, which radiate outside of the slab [53]. These guided modes in the band diagram of a photonic crystal exist outside the light cone, which defines the boundary between the guided modes and radiation modes. It has been proven in previous reports that the investigated PNC resembles the photonic crystal slabs where the pillar array over the substrate corresponds to the slab region [36]. Moreover, the guided surface modes (bands) also exist outside the sound cone in the band diagram, and the related band gaps are assumed as the frequency range where no guided modes exist.

Figure 2(a) indicates the unit cell of the investigated perfect PNC and part (b) displays the related Brillouin zone of the lattice. Figures 3(a)–3(d) display the band structures of the perfect PNCs with different pillar radius (r) values of 45, 65, 80, and 95 nm, while $a = 200$ nm and $h/a = 0.5$. This figure presents the high dependency of local-resonance band gaps on the filling factor of the PNC. The gray region in the dispersions highlights the sound cone, which represents the radiative zone to the Si substrate, which distinguishes the bulk modes from the surface-coupled modes of the elastic waves. The cone boundaries are achieved by calculating the smallest elastic bulk wave phase velocity in Si along different propagation directions. The sound line along the ΓX direction is calculated by the smallest elastic wave velocity in Si in the ΓX direction, which is a shear horizontal wave velocity of $\sqrt{(c_{44}/\rho)}$, and for the ΓM direction, the quasishear

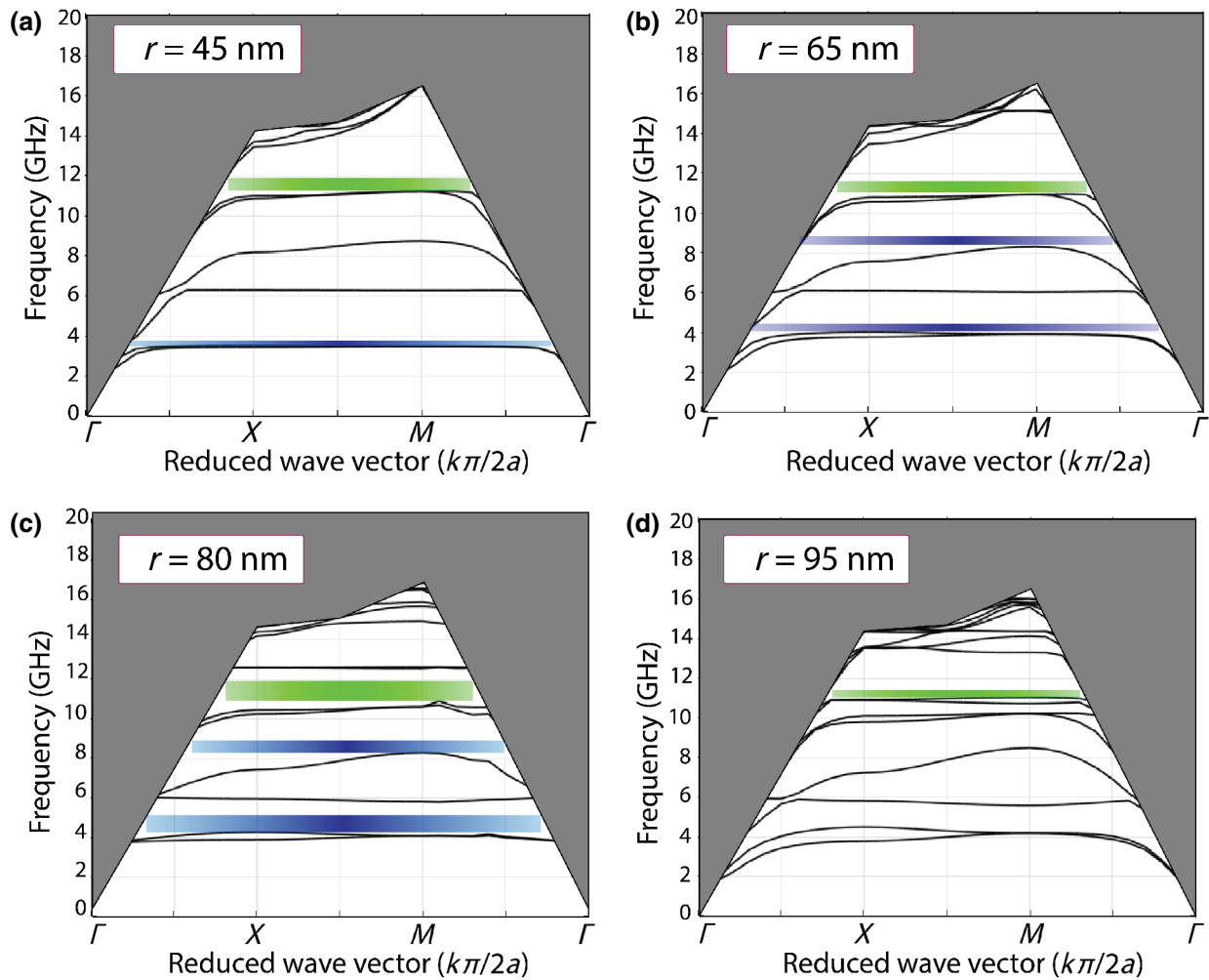


FIG. 3. Band structures of perfect PNCs consisting of ZnO pillars with $h/a = 0.5$ and different r values of: (a) 45 nm, (b) 65 nm, (c) 85 nm, and (d) 95 nm.

horizontal wave velocity defined by $\sqrt{(c_{11} - c_{12})/\rho}$ is utilized to calculate the sound cone boundary [36]. The observed band gaps are highlighted by blue ribbons in the band structures. The high-frequency band gap of around 12 GHz (green gap) is the Bragg gap that is nearly present for all four r values and does not vary significantly with the structural parameters of the pillars, since the PNC lattice constant is kept constant and the Bragg band-gap frequency depends on it. The other lower frequency gaps (blue gaps) are the local-resonance gaps, which occur at wavelengths higher than the distances between the pillars. These band gaps are created by the local resonance of the pillars coupled with the SAWs. The observed local-resonance gaps in Fig. 3 are emerging from $r = 45$ nm, then increasing and widening to $r = 80$ nm and fading for $r = 95$ nm. For $r = 45$ nm, the first gap occurs between $f = 3.48$ to 3.75 GHz with a relative bandwidth of 7.1% and the Bragg band gap (green gap) occurs from $f = 11.24$ to 11.4 GHz with a relative bandwidth of 5.2%.

For $r = 65$ nm, the first band gap (blue gap) occurs from $f = 4.14$ to 4.48 GHz with a relative bandwidth of 7.9%, the second band gap (blue gap) occurs from $f = 8.35$ to 8.8 GHz with a relative bandwidth of 5.24%, and the Bragg band gap (green gap) occurs from $f = 11$ to 11.58 GHz with a relative bandwidth of 5.13%. For $r = 80$ nm, the first band gap (blue gap) occurs from $f = 4.31$ to 5.16 GHz with a relative bandwidth of 17%, the second band gap (blue gap) occurs from $f = 8.25$ to 8.875 GHz with a relative bandwidth of 8.8%, and the Bragg band gap (green gap) occurs from $f = 10.87$ to 11.87 GHz with a relative bandwidth of 8.8%. Finally, for $r = 95$ nm, only the Bragg band gap (green gap) occurs from $f = 11$ to 11.375 GHz with a relative bandwidth of 3.3% and no local-resonance gaps exist.

The observed band-gap widening from $r = 45$ to $r = 80$ nm is attributed to the improved surface coupling between the pillars [36]. It should be noted here that the resonance frequencies of the pillars depend on the

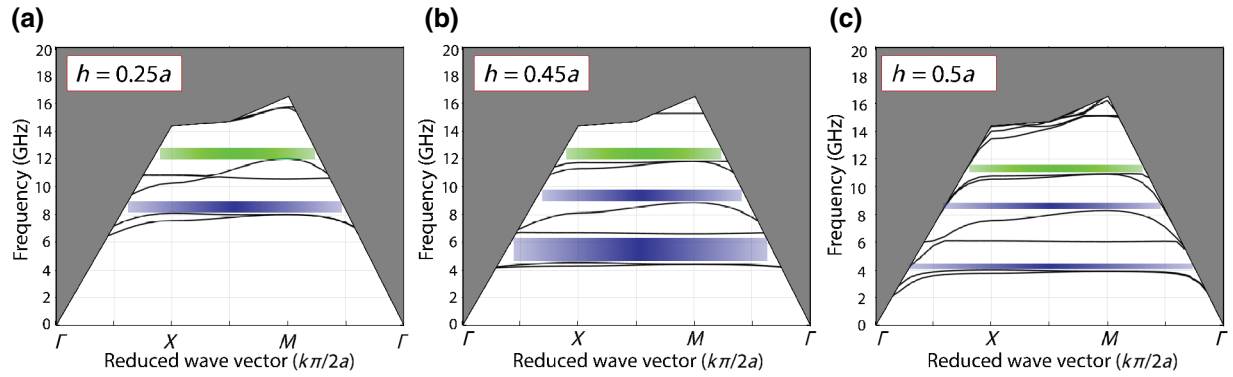


FIG. 4. Band structure of a perfect PNC consisting of ZnO pillars with $r = 65$ nm for different h/a values of: (a) 0.25, (b) 0.45, and (c) 0.5. Bragg and local resonance band gaps are highlighted by green and blue ribbons, respectively.

mechanical parameters of the resonators. These resonators can be simplified by a spring-mass model, so that the spring stiffness and mass of the resonators affect their resonance frequency ($f \propto \sqrt{k/m}$), and thus the frequency of the local resonance-coupled modes. Whenever the radii of the pillars start to increase, the mass and spring stiffness start to increase as well, leading to a competing effect on the local resonance frequencies. The overall behavior of these two effects can lead to a dominant effect of increasing mass, a downshift of resonance frequencies, and the appearance of surface-coupled modes in lower frequency ranges, such that band gaps show up vs increasing r for $r \leq 80$ nm. But for r values higher than 80 nm, it seems that the effect of spring stiffness dominates, the resonance frequencies upshift, and the low-frequency band gaps close. Furthermore, the upper limit of the increasing radii can be assumed as a ZnO continuum layer on the substrate in which multiple surface bands replace the local resonance-coupled bands in the low-frequency range, and as a result, neither local-resonance gaps nor a Bragg gap will exist.

Figure 4(a)–4(c) indicate the effect of the pillar’s aspect ratio (h/a) on the band structure of the investigated perfect PNCs for $h/a = 0.25, 0.45,$ and 0.5 , respectively, while $r = 65$ nm and $a = 200$ nm. For $h/a = 0.25$, the first band gap (blue gap) occurs from $f = 8.125$ to 8.96 GHz with a relative bandwidth of 9.8% and the Bragg band gap occurs from $f = 12$ to 12.83 GHz with a relative bandwidth of 6.7%. For $h/a = 0.45$, the first band gap (blue gap) occurs from $f = 4.6$ to 6.32 GHz with a relative bandwidth of 31.5%, the second band gap (blue gap) occurs from $f = 8.87$ to 9.7 GHz with a relative bandwidth of 9%, and the Bragg band gap (green gap) occurs from $f = 12$ to 12.83 GHz with a relative bandwidth of 6.6%. The band-gap frequencies and relative bandwidth for $h/a = 0.5$ in Fig. 4(c) are the same as in Fig. 3(b). It can be observed that the higher frequency band gap is not influenced by the h/a value, which confirms its Bragg gap characteristic (green gap). However, the lower frequency gaps downshift and widen for the higher h/a value, so that they can

be attributed to local-resonance gaps (blue gaps). Again, the pillars can be assumed to act as springs attached to the substrate, thus the spring resonance frequency and the resulting local-resonance gap downshifts for longer pillars. It should be noted here that increasing h and keeping a constant is equal to increasing the mass while decreasing the spring stiffness of the spring-mass system, where both affect the resonance frequencies. Hence, a higher h value results in lower resonance frequencies and downshifted local resonance-coupled bands and local-resonance gaps. Moreover, the emerged additional local resonance gap for $h/a = 0.45$ can be related to the higher-order resonance modes of longer pillars.

It should be noted that structural parameters of $r = 65$ nm and $h/a = 0.5$ correspond to a feasible ZnO thickness of around 100 nm, which is well below the UV penetration depth, and these show an acceptable low-frequency local-resonance gap width for shear-horizontal SAWs. Regarding this, we choose these structural parameters for the proposed PNC-based SAW device. Figure 5 illustrates the related band structure [part (a)], the magnified band structure in the ΓX direction [left pane of part (b)], and the transmission spectra for Rayleigh and shear-horizontal incident waves. The utilized super cell with 11 pillars for calculating the transmission spectra is presented in Fig. 2(c). Figure 5(b) reveals that the transmission gaps are in good agreement with the gaps in the band structure.

To clarify the correspondence of the observed Rayleigh and shear-horizontal transmissions to the band structure, we consider the displacement components of the modes at the X point (not shown), which reveal that the first six bands (numbered from the bottom to top of the dispersion) respond to either sagittal or transverse excitation. In other words, the first, third, and fifth bands respond mostly to the incident transversely polarized wave, while the second, fourth, and sixth bands respond mostly to the incidently sagittal-polarized wave. For instance, the third band (mode A) in the dispersion shows considerable x and y displacement components, while the x component

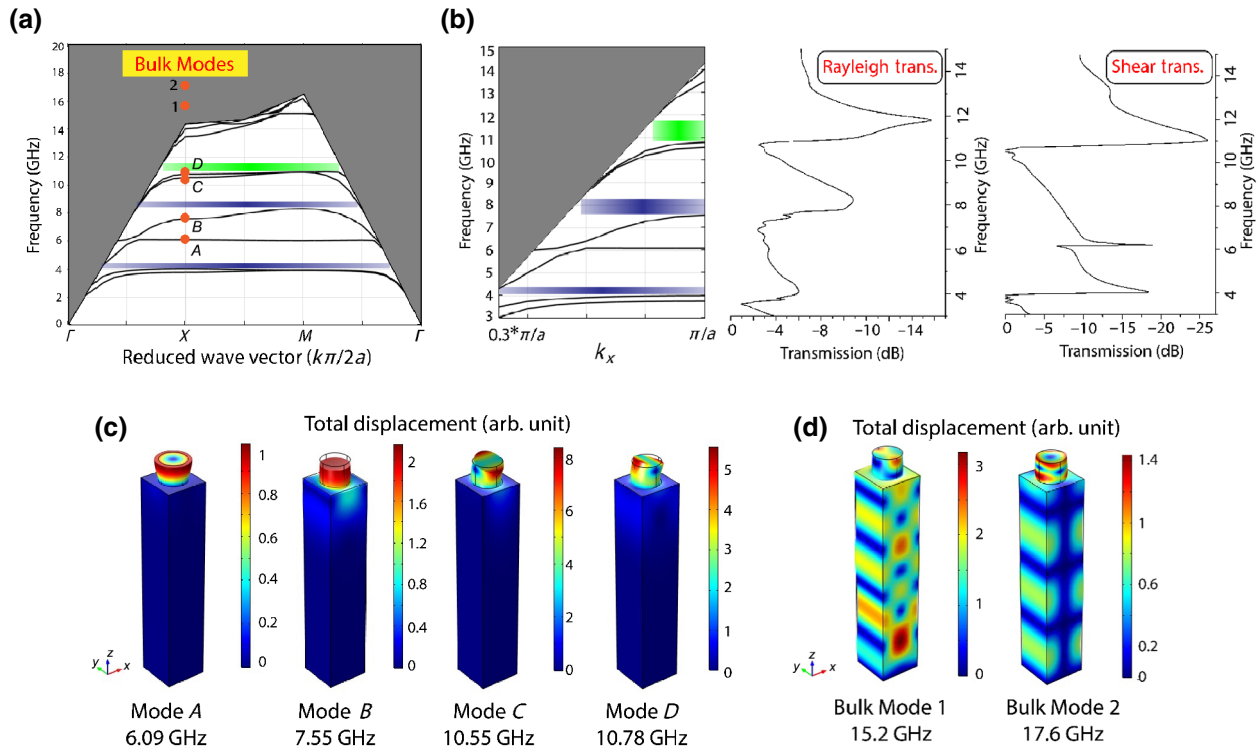


FIG. 5. (a) The band structure of a perfect PNC consisting of ZnO pillars with $r = 65$ nm and $h/a = 0.5$. Bragg and local resonance band gaps are highlighted by green and blue ribbons, respectively. (b) Band structure in the ΓX direction beside the transmission spectra of Rayleigh and shear-horizontal waves. The total displacement as well as the deformation shapes for: (c) the selected A , B , C , and D surface coupled modes and (d) for the selected bulk modes (mode no. 1 and mode no. 2) in the band structure.

is antisymmetric with respect to the sagittal mid plane (x, z), but the y component is symmetric. Thus, the sagittal source cannot transfer energy to the third band, while shear-horizontal excitation transfers energy to this band. In other words, the third band is absent in the sagittal transmission spectrum and results in a transmission dip; but it leads to a transmission relative peak in the shear-horizontal spectrum. Moreover, the fourth band (B mode) shows dominant sagittal polarization and is absent (corresponding to the transmission dip) in the shear-horizontal transmission spectrum, while it corresponds to the observed relative peak in the Rayleigh transmission. Thus, the second dips for the Rayleigh and shear-horizontal transmissions start at around 7 and 6 GHz, corresponding to the upper edge of the fourth and the third bands, respectively. Moreover, the fifth band (C mode) shows dominant y and z components, which are symmetric and antisymmetric with respect to the sagittal mid plane, respectively. Hence, a sagittal source cannot transfer energy to this band, but this band can be excited by a shear-horizontal source, thus showing high transmission in the shear-horizontal spectrum. The sixth band (D mode) shows high z and x components of displacement, which is a sign of dominant sagittal polarization, but is absent in shear-horizontal transmission. Considering the near frequency behavior of the latter two

bands (fifth and sixth bands), the corresponding dips are near in the sagittal and shear horizontal transmission spectra, as is observed in Fig. 5(b). Total displacements and the deformation shapes of the four selected surface modes (A , B , C , and D) are depicted in Fig. 5(c) to illustrate the interaction of surface wave modes and resonance modes of the pillars as well as the dominant polarization of the bands. Moreover, Fig. 5(d) manifests the total displacement and the deformation shape in a single unit cell for the selected bulk modes (mode no.1 and no.2) labeled in part (a). This shows that displacement is confined to the pillars and the pillar/Si interface for surface modes, however, it completely radiates into the bulk for bulk modes.

B. Linear pillar defect in PNC

Now, we study the waveguiding behavior of a PNC with a linear defect of the pillars. Here, we introduce a line defect consisting of pillars with different radii from the rest of PNC, so that elastic energy can be confined inside the defect, leading to the creation of defect modes with slow group velocities. Figure 2(d) displays the related supercell consisting of 11 pillars with a middle defect pillar. Figure 6 exhibits the band structures relating to $r = 65$ nm, $a = 200$ nm, and $h/a = 0.5$, while a line defect of pillars

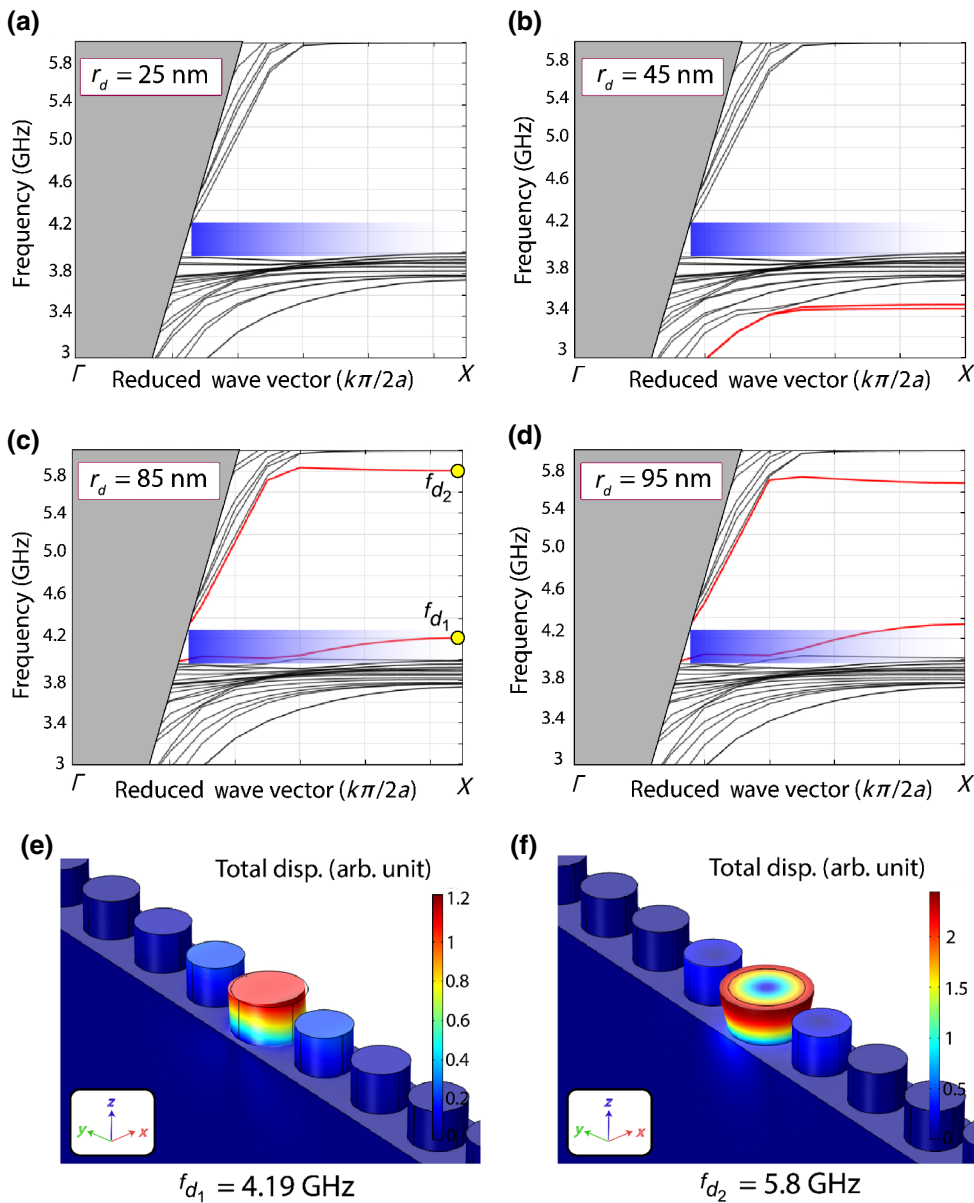


FIG. 6. The band structures of PNCs with linear pillar defects of r_d values equal to: (a) 25 nm, (b) 45 nm, (c) 85 nm, and (d) 95 nm. The local-resonance band gap is highlighted by a blue ribbon and defect bands are shown by red bands. Total displacement and the deformation shapes corresponding to the X point of defect bands in part (c) for (e) $f_{d1} = 4.19$ GHz and (f) $f_{d2} = 5.8$ GHz.

with different defect radii ($r_d = 25, 45, 85,$ and 95 nm) is introduced to the PNC. For $r_d = 25$ nm, the defect band is out of the presented band structure frequency range and is obviously placed well outside the band gap (blue ribbon) in Fig. 6(a). Defect bands (red bands) are shown out of the local-resonance band gap for $r_d = 45$ nm. Then, a highly dispersive defect band enters the gap for $r_d = 85$ nm, and partially exits the gap for $r_d = 95$ nm. Figures 6(e) and 6(f) present the total displacement and deformation shape of the defect bands of part (c) (f_{d1} and f_{d2}) near the X point of the first Brillouin zone, which confirms the localization of the elastic wave to the defect pillars. The worthy point here is that introducing a linear defect based on pillars to the PNC allows the creation of SAW modes in the local resonance gap by engineering the r_d value. However, the bandwidth of the created defect modes is achieved to

be comparable to the local-resonance gap width [54,55]. In other words, the created defect bands inside the band gap are so dispersive that they can even close the local-resonance gap. The observed behavior of the defect bands prevents designing high-quality-factor SAW devices, such as band-pass filters. In other words, it is observed in this figure that lower r_d values, such as $r_d = 45$ nm, lead to a nearly flat and narrow defect band [part (b)], because reducing the radius of a pillar defect as a resonating spring can reduce the allowed resonance frequency bandwidth.

In order to conduct the defect bands into the local-resonance gap, increasing r_d is inevitable, as shown in Fig. 6. However, as a result of higher resonance frequency bandwidth, a defect pillar with a high r_d value leads to the formation of dispersive defect bands. Hence, there is a contradictory behavior between the in-gap defect frequency

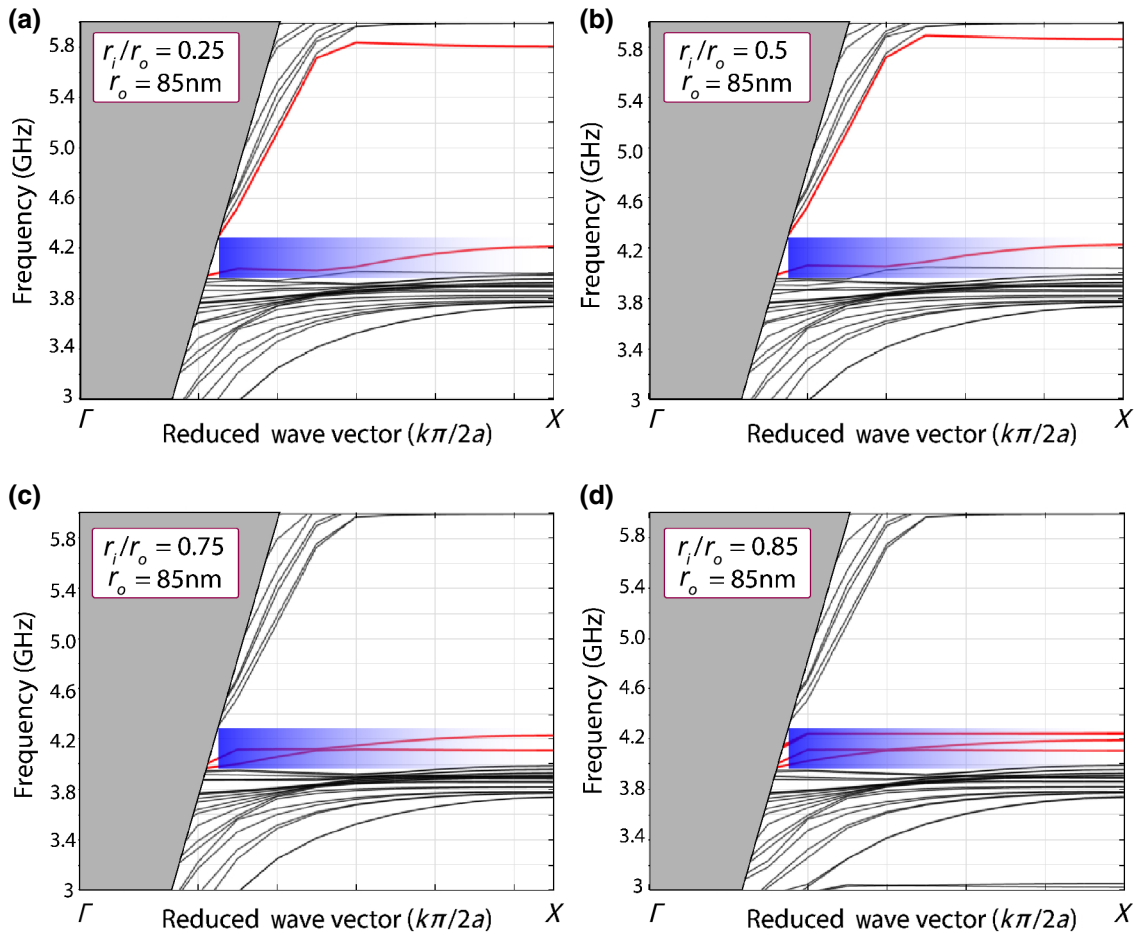


FIG. 7. The band structure of a PNC with linear hollow cylinder defects with $r_o = 85$ nm and r_i/r_o values equal to: (a) 0.25, (b) 0.5, (c) 0.75, and (d) 0.85. The local-resonance band gap is highlighted by a blue ribbon and defect bands are shown by red bands.

position and the narrow bandwidth of the guiding mode for the linear pillar defect in the proposed PNC.

C. Linear hollow cylinder defect in the PNC

To achieve a higher degree of freedom in tailoring defect behavior and gain defect modes inside the gap with a bandwidth lower than the gap width, we introduce a linear defect consisting of hollow cylinders. In hollow cylinders, the effective radii of the pillar defects are reduced so that flat defect bands can be achieved, while defect bands can be conducted into the gap by benefiting from the additional structural degrees of freedom. We show that the proposed defect structure allows the realization of near-flat defect bands around the middle of the local-resonance band gaps by controlling the inner radius (r_i) and outer radius (r_o) of the hollow cylinders. Moreover, it is notable that replacing the pillar defects with hollow cylinders does not involve any additional fabrication process step and complication to the system.

To elaborate on the defect band behavior of the hollow cylinder defects, first, we study the effect of varying r_i/r_o

from 0.25 to 0.85 on the band structure of the defected PNC in Fig. 7, when $r_o = 85$ nm. Similar to the previous subsection, the band gaps are highlighted by blue ribbons and the defect bands are shown by red bands in the band structures. As expected, a low r_i/r_o value ($r_i/r_o = 0.25$) shows a similar band structure as the pillar defect results with $r_d = 85$ nm [Fig. 6(c)]. In addition, it is observable in Fig. 7 that a higher r_i/r_o leads to discretization of the resonance frequencies and creation of a higher number of flat defect bands. This observation is attributed to the spatial confinement of elastic waves in the hollow cylinders with higher r_i/r_o values in comparison with that of the pillars. A pillar can be assumed to be a summation of hollow cylinders with sequential r_o values and the same center point. As a consequence, the pillar defect bands can be assumed as a superposition of the hollow cylinder defect bands. This description explains the higher width of a pillar defect's band than that of a hollow cylinder. However, it should be noted that the higher number of defect bands compromises the flattening of each defect band for higher r_i/r_o values in order to achieve a transmission bandwidth lower than the local-resonance gap width for the designed

SAW filter. Hence, we choose $r_i/r_o = 0.85$ [Fig. 7(d)] to investigate the effect of r_o on the defect bands in the next part. Our main goal is to achieve a fewer number of flat defect bands near the mid gap. In other words, we optimize the structural parameters of the hollow cylinders

to achieve an acceptable narrow-band waveguiding (or filtering) operation inside the local resonance gap.

Now, we present the effect of varying r_o (45, 65, 85 and 95 nm) of the hollow cylinder defects on the band structure in Figs. 8(a)–8(d), while $r_i/r_o = 0.85$. It is observable here

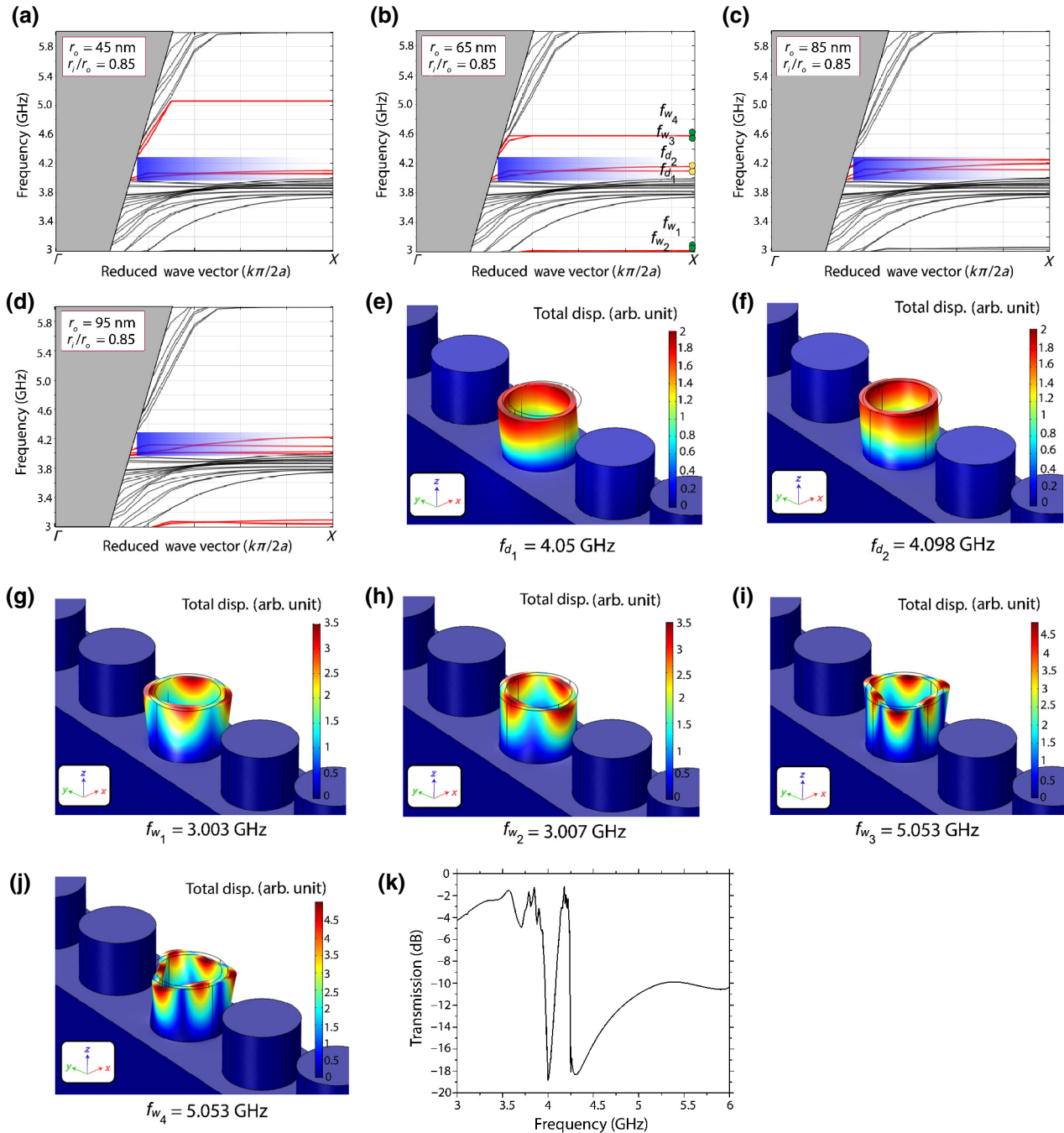


FIG. 8. The band structure of a PNC with linear hollow cylinder defects of $r_i/r_o = 0.85$ and r_o values equal to: (a) 45 nm, (b) 65 nm, (c) 85 nm, and (d) 95 nm. The local-resonance band gap is highlighted by a blue ribbon and defect bands are shown by red bands. Total displacement and the deformation shapes corresponding to the X point of defect bands highlighted in part (b). Defect modes inside the band gap: (e) $f_{d1} = 4.06$ GHz, (f) $f_{d2} = 4.1$ GHz. Whispering gallery modes outside the bandgap: (g) $f_{w1} = 3.03$ GHz, (h) $f_{w2} = 3.07$ GHz, (i) $f_{w3} = 5.05$ GHz, and (j) $f_{w4} = 5.053$ GHz. (k) Shear-horizontal transmission spectrum for a hollow cylinder defect corresponding to the dispersion of part (b).

that increasing r_o leads to a greater number of defect bands and a wider defect bandwidth as a consequence, which is related to the increase of allowed resonance modes in cylinders with higher volumes. Therefore, we discard $r_o \geq 65$ nm and select $r_o = 65$ nm to design the desired waveguide with a narrow bandwidth defect-induced transmission. In Figs. 8(e) and 8(f), we demonstrate the total displacement as well as the deformation shape of two defect guiding frequencies in the band gap, f_{d_1} and f_{d_2} , in the vicinity of the X point of part (b). It can be observed that the hollow cylinders keep their round shapes in these guiding modes. However, the hollow cylinders also create a set of whispering gallery modes in which the round forms of the cylinders are changed to elliptical and higher-order deformation shapes. In these modes, the acoustic wave travels around the hollow cylinder side walls and perturbs its shape and form. Whenever r_o and r_i/r_o values increase, a higher number of whispering gallery modes will be present due to the increased acoustic path for the travelling wave around the cylinder walls. Whispering gallery modes with defect frequencies of f_{w_1} , f_{w_2} , f_{w_3} , and f_{w_4} are present outside the band gap in the dispersion of our structure as labeled in Fig. 8(b). The deformation shape and total displacement of these whispering gallery modes are presented in parts (g–j) of Fig. 8. These results confirm the localization of an incident elastic wave to the hollow cylinders for the waveguiding defect frequencies. Moreover, it is observable that the deformation shapes corresponding to the defect frequencies inside the band gap, f_{d_1} and f_{d_2} , show almost transverse polarization. Additionally, the shear-horizontal wave transmission shows a significant dip around the lower frequency local-resonance gap (around 4 GHz), as seen in Fig. 5(b). Hence, we present the shear-horizontal transmission spectrum for this line defect, made of intrinsic ZnO structures, in Fig. 8(k). Hereafter, we focus on the shear-horizontal wave for the proposed SAW filter, which also benefits from a high effective electromechanical coupling factor and high energy concentration near the metallized surface of the shear-horizontal SAW devices. This design currently has wide applications in wireless communications systems such as mobile phone networks [45].

In order to confirm the effect of the structural parameters (r_i/r_o and r_o) of hollow cylinders on the resulting filtering behavior, transmission spectra of the corresponding PNCs are calculated and investigated. Figure 9 summarizes the effects of varying r_i/r_o on the output transmission of the filter, including the defect transmission frequency (f_d) and full width at half maximum (FWHM) of the related defect transmission peaks, for different r_o values. In this figure, FWHM values are shown as error bars around defect peak frequencies. The green dotted level represents the mid-gap level (E_i), and the gray bottom and top regions display the transmission zones where the band gap lies between them.

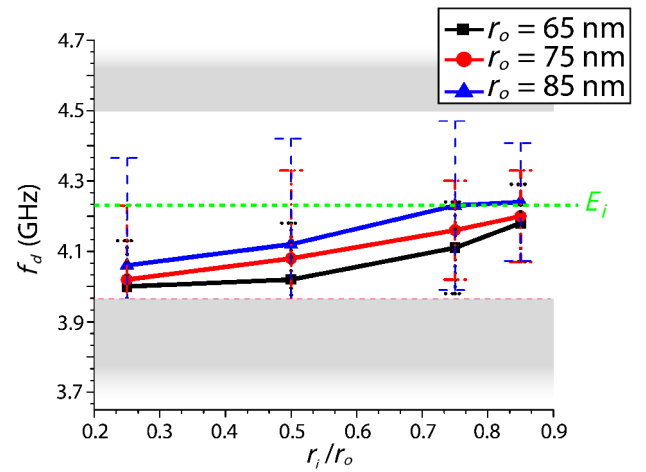


FIG. 9. Variation of f_d with respect to r_i/r_o for different r_o values (65, 75, and 85 nm). FWHM values of the corresponding transmission peaks are presented by error bars. The mid-gap level is shown by a dashed green line and the band gap is restricted by the gray zones (pass bands).

It is evident that increasing r_i/r_o results in upshifting f_d from the bottom gap edge to the mid-gap frequency. This upshifting is in agreement with higher resonance frequencies for resonating springs with lower mass at higher r_i/r_o . The other noteworthy point in this figure is the variation of FWHM vs r_i/r_o and r_o , which is in accordance with the discussed trade off between the number of defect bands and transmission peak broadening. It can be seen that for $r_i/r_o \leq 0.5$, there exist FWHM values comparable with the band gap (E_g), so that transmission peaks merge with the transmission edge and are evidently not favorable for filtering behavior. Thus, we select $r_i/r_o = 0.85$ and $r_o = 65$ nm as the optimum structural parameters for the designed SAW filter, where f_d is located at the vicinity of the mid gap and the FWHM is lower than the $E_g/2$.

D. Tunable defect modes by acoustoelectric interaction

First, we clarify the applied assumptions and approximations for simulating acoustoelectric-induced behavior of the defect modes in the designed waveguide (filter) based on a linear defect of the hollow cylinders. The required conductivity modulation for the presented tunable filter is realized by exposing the ZnO-based PNC to UV illumination. It can be estimated that UV illumination with a power density of about 80 mW/mm² and an incident wavelength of 365 nm can raise the conductivity of the intrinsic ZnO layer to 100 S/m. Therefore, the required conductivity modulation can be realized by means of a feasible illumination power density of an UV source. On the other hand, we assume the height of the pillars and cylinders to be equal to 100 nm, which is well below the penetration depth of UV in ZnO. Hence, we approximate a uniform

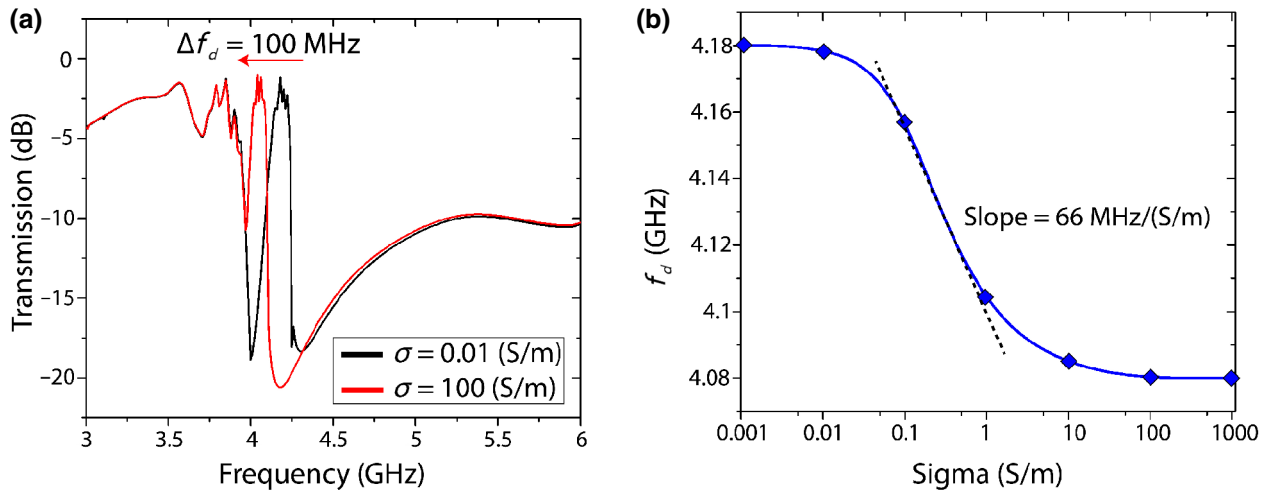


FIG. 10. (a) Transmission spectra of the PNC with a linear hollow cylinder defect of $r_o = 65$ nm and $r_i/r_o = 0.85$ for two different σ values of 0.01 S/m (black spectrum) and 100 S/m (red spectrum). (b) Modulation of f_d with variation of σ in the ZnO structures.

conductivity modulation along the height of the pillars and cylinders in the designed PNC-based filter.

We numerically investigate the impact of conductivity variation in the operation of a designed filter by modulating the elastic parameters of ZnO structures through Eqs. (7) and (8). Figure 10(a) presents the transmission spectra for a shear-horizontal wave of the designed filter based on hollow cylinder defects with $r_i/r_o = 0.85$ and $r_o = 65$ nm for two different σ values. It is evident that the transmission spectrum for low conductivity (black spectrum) is similar to the spectrum corresponding to that of intrinsic ZnO, as shown in Fig. 8(k). Increasing σ from 0.01 to 100 S/m in the ZnO structures results in a red shift (Δf_d) of about 100 MHz for $f_d = 4.18$ GHz due to the acoustoelectric interaction in ZnO-based PNC. It is obvious that the bandwidth of the designed filter in the GHz range is about 100 MHz, and the frequency shift is comparable with the bandwidth, revealing a high tunability for the designed SAW filter, which can be suitable for wireless communication applications such as duplexers [27,45]. To elaborate the observed tunable behavior, it should be noted that generation of excess carriers in ZnO can screen the electric field associated with the traveling elastic wave, or equivalently, can lead to some kind of electrostatically induced modulation of the interatomic springs and modulation of elastic constants of the ZnO-based hollow cylinder resonators. This modulation of the elastic parameters in defect structures leads to a modulation of the resonance frequency of hollow cylinders and to the surface modes coupled with the defect resonances. This modulation of elastic parameters is applied to all the ZnO structures, including PNC pillars and the line of hollow cylinders. However, Fig. 10(a) reveals that the guiding frequency is modulated by conductivity modulation, while the whole spectrum and the observed transmission dip do

not change significantly. Part (b) in this figure presents the calculated variation of f_d vs varying σ , revealing the maximum tunability of $\Delta f_d/\Delta\sigma = 66$ MHz/(S/m) around $f_d = 4.13$ GHz, as shown by the dashed line. The achieved tunability is valid for a specific range of conductivity and out of this range, the tunability shows a saturation behavior that is in good agreement with the previously reported SAW velocity modulation as a consequence of the acoustoelectric effect [47,51]. The proposed tunable SAW filter shows promising potential for a new generation of reconfigurable SAW devices with wide application fields, such as rf filters and duplexers.

V. CONCLUSION

A PNC of ZnO pillars over a Si substrate in a square lattice structure is introduced and investigated. The local-resonance band gaps and surface coupled modes are probed for different structural parameters of PNC. Moreover, in order to introduce a narrow-band waveguiding, a linear defect of hollow cylinders is tailored inside the PNC. Through numerical investigations, the structural parameters of hollow cylinders are optimized to achieve improved performance, consisting of narrow-band guiding modes near the mid gap of the PNC with transmission bandwidth below the gap width. Taking advantage of the acoustoelectric effect in modulating the optimized guiding frequency, we prove a maximum tunability of the guiding transmission peak of about $\Delta f_d/\Delta\sigma = 66$ MHz/(S/m). The proposed acoustoelectric interaction can be practically implemented by contactless UV illumination. The designed tunable rf filter is a shear-horizontal band-pass SAW filter at $f_d = 4.13$ GHz and a bandwidth of about 100 MHz. The resulting frequency shift can be comparable with the bandwidth, which can be suitable for wireless

communication applications such as reconfigurable rf filters or duplexers, benefiting from simple and CMOS-compatible fabrication processes.

ACKNOWLEDGMENTS

The authors acknowledge the partial financial support of the Iran National Science Foundation (Grant No. INSF#97010601), and the financial support from Tarbiat Modares University through Grant No. IG-397.

-
- [1] V. Narayanamurti, H. L. Störmer, M. A. Chin, A. C. Gosard, and W. Wiegmann, Selective Transmission of High-Frequency Phonons by a Superlattice: The “Dielectric” Phonon Filter, *Phys. Rev. Lett.* **43**, 2012 (1979).
- [2] M. S. Kushwaha, P. Halevi, L. Dobrzynski, and B. Djafari-Rouhani, Acoustic Band Structure of Periodic Elastic Composites, *Phys. Rev. Lett.* **71**, 2022 (1993).
- [3] F. R. Montero de Espinosa, E. Jiménez, and M. Torres, Ultrasonic Band Gap in a Periodic Two-Dimensional Composite, *Phys. Rev. Lett.* **80**, 1208 (1998).
- [4] S. Mohammadi, A. Eftekhar, A. Khelif, W. Hunt, and A. Adibi, Evidence of large high frequency complete phononic band gaps in silicon phononic crystal plates, *Appl. Phys. Lett.* **92**, 221905 (2008).
- [5] R. Chaunsali, F. Li, and J. Yang, Stress wave isolation by purely mechanical topological phononic crystals, *Sci. Rep.* **6**, 30662 (2016).
- [6] A. Khelif, A. Choujaa, S. Benchabane, B. Djafari-Rouhani, and V. Laude, Guiding and bending of acoustic waves in highly confined phononic crystal waveguides, *Appl. Phys. Lett.* **84**, 4400 (2004).
- [7] R. Lucklum and J. Li, Phononic crystals for liquid sensor applications, *Meas. Sci. Tech.* **20**, 12 (2008).
- [8] R. Lucklum, Phononic crystals and metamaterials - promising new sensor platforms, *Procedia. Eng.* **87**, 40 (2014).
- [9] S. Mohammadi, Ph.D. Thesis: Georgia Institute of Technology, 2010.
- [10] Y. Pennec, B. Djafari-Rouhani, J. O. Vasseur, A. Khelif, and P. A. Deymier, Tunable filtering and demultiplexing in phononic crystals with hollow cylinders, *Phys. Rev. E* **69**, 046608 (2004).
- [11] B. Rostami-Dogolsara, M. Moravvej-Farshi, and F. Nazari, Designing switchable phononic crystal-based acoustic demultiplexer, *IEEE Trans. Ultrason. Ferroele. Freq. Cont.* **63**, 9 (2016).
- [12] S. Mohammadi, A. Eftekhar, and A. Adibi, in 2010 IEEE. Int. Freq. Con. Sym (2010), Vol. 521.
- [13] Z. Liu, X. Zhang, Y. Mao, Y. Y. Zhu, Z. Yang, C. T. Chan, and P. Sheng, Locally resonant sonic materials, *Science* **289**, 5485 (2000).
- [14] M. Javadi, A. Heidari, and S. Darbari, Realization of enhanced sound-driven CNT-based triboelectric nanogenerator, utilizing sonic array configuration, *Cu. Appl. Phys.* **18**, 361 (2018).
- [15] A. Shakeri, S. Darbari, and M. K. Moravvej-Farshi, Designing A tunable acoustic resonator based on defect modes stimulated by selectively biased PZT rods in a 2D phononic crystal, *Ultrasonics* **92**, 8 (2019).
- [16] M.-H. Lu, L. Feng, and Y.-F. Chen, Phononic crystals and acoustic metamaterials, *Mater. Today* **12**, 34 (2009).
- [17] D. M. Profunser, E. Muramoto, O. Matsuda, O. B. Wright, and U. Lang, Dynamic visualization of surface acoustic waves on a two-dimensional phononic crystal, *Phys. Rev. B* **80**, 014301 (2009).
- [18] B. Liang, B. Yuan, and J. C. Cheng, Acoustic Diode: Rectification of Acoustic Energy Flux in One-Dimensional Systems, *Phys. Rev. Lett.* **103**, 104301 (2009).
- [19] M. Maldovan, Sound and heat revolutions in phononics, *Nature* **503**, 209 (2013).
- [20] L. Rayleigh, On Waves propagated along the plane surface of an elastic solid, *Proc. London. Math. Soc.* **s1–17**, 4 (1885).
- [21] R. White and F. Voltmer, Direct piezoelectric coupling to surface elastic waves, *Appl. Phys. Lett.* **7**, 314 (1965).
- [22] C. W. Ruppel, Acoustic wave filter technology - A Review, *IEEE Trans. Ultrason. Ferroele. Freq. Cont.* **64**, 2690905 (2017).
- [23] M. Lewis, in 1982 Ultrason. Sym. (1982), Vol. 12.
- [24] M. Hikita, Y. Kinoshita, H. Kojima, and T. Tabuchi, Resonant s.a.w. filter using surface shear wave mode on LiTaO₃ substrate, *Electron. Lett.* **16**, 446 (1980).
- [25] M. Hikita, Y. Ishida, T. Tabuchi, and K. Kurosawa, Miniature SAW antenna duplexer for 800-MHz portable telephone used in cellular radio systems, *IEEE Trans. Microwave Theory Tech.* **36**, 1047 (1988).
- [26] J. Tsutsumi, S. Inoue, Y. Iwamoto, T. Matsuda, M. Miura, Y. Satoh, M. Ueda, and O. Ikata, in IEEE Frequency Control Symp. (2003), Vol. 861.
- [27] M. Kadota, T. Nakao, N. Taniguchi, E. Takata, M. Mimura, K. Nishiyama, T. Hada, and T. Komura, Surface acoustic wave duplexer for US personal communication services with good temperature characteristics, *Jpn. J. Appl. Phys.* **44**, 6B (2005).
- [28] B. Liu, X. Chen, H. Cai, M. Mohammad Ali, X. Tian, L. Tao, Y. Yang, and T. Ren, Surface acoustic wave devices for sensor applications, *J. Semicond.* **37**, 2 (2016).
- [29] L. Rana, R. Gupta, M. Tomar, and V. Gupta, ZnO/ST-Quartz SAW resonator: An efficient NO₂ gas sensor, *Sens. Actu. B: Chem.* **252**, 840 (2017).
- [30] T. Aubert, O. Elmazria, B. Assouar, L. Bouvot, and M. Oudich, Surface acoustic wave devices based on AlN/sapphire structure for high temperature applications, *Appl. Phys. Lett.* **96**, 203503 (2010).
- [31] M. Kadota, S. Ito, Y. Ito, T. Hada, and K. Okaguchi, Magnetic sensor based on surface acoustic wave resonators, *Jpn. J. Appl. Phys.* **50**, 07HD07 (2011).
- [32] V. Polewczyk, K. Dumesnil, D. Lacour, M. Moutaouekkil, H. Mjahed, N. Tiercelin, S. Petit Watelot, H. Mishra, Y. Dusch, S. Hage-Ali, O. Elmazria, F. Montaigne, A. Talbi, O. Bou Matar, and M. Hehn, Unipolar and Bipolar High-Magnetic-Field Sensors based on surface acoustic wave resonators, *Phys. Rev. Appl.* **8**, 024001 (2017).
- [33] S. Mohammadi, A. Eftekhar, A. Khelif, H. Moubchir, R. Westafer, W. Hunt, and A. Adibi, Complete phononic bandgaps and bandgap maps in two-dimensional silicon phononic crystal plates, *Electron. Lett.* **43**, 898 (2007).

- [34] C. Goffaux, J. Sanchez-Dehesa, A. Levy Yeyati, P. Lambin, A. Khelif, J. O. Vasseur, and B. Djafari-Rouhani, Evidence of Fano-Like Interference phenomena in locally resonant materials, *Phys. Rev. Lett.* **88**, 225502 (2002).
- [35] Y. Pennec, B. Djafari-Rouhani, H. Larabi, J. O. Vasseur, and A. C. Hladky-Hennion, Low-frequency gaps in a phononic crystal constituted of cylindrical dots deposited on a thin homogeneous plate, *Phys. Rev. B* **78**, 104105 (2008).
- [36] A. Khelif, Y. Achaoui, S. Benchabane, V. Laude, and B. Aoubiza, Locally resonant surface acoustic wave band gaps in a two-dimensional phononic crystal of pillars on a surface, *Phys. Rev. B* **81**, 214303 (2010).
- [37] Y. Achaoui, A. Khelif, S. Benchabane, L. Robert, and V. Laude, Experimental observation of locally-resonant and Bragg band gaps for surface guided waves in a phononic crystal of pillars, *Phys. Rev. B* **83**, 104201 (2011).
- [38] B. Ash, S. Worsfold, P. Vukusic, and G. Nash, A Highly attenuating and frequency tailorable annular hole phononic crystal for surface acoustic waves, *Nat. Commun.* **8**, 174 (2017).
- [39] J. Vasseur, A. Hladky-Hennion, B. Djafari-Rouhani, F. Duval, B. Dubus, Y. Pennec, and P. Deymier, Waveguiding in two-dimensional piezoelectric phononic crystal plates, *J. Appl. Phys.* **101**, 114904 (2007).
- [40] S. Benchabane, O. Gaiffe, R. Salut, G. Ulliac, V. Laude, and K. Kokkonen, Guidance of surface waves in a micron-scale phononic crystal line-defect waveguide, *Appl. Phys. Lett.* **106**, 081903 (2015).
- [41] Y. Guo, M. Schubert, and T. Dekorsy, Guidance of surface elastic waves along a linear chain of pillars, *J. Appl. Phys.* **119**, 124302 (2016).
- [42] J. Luo, A. Quan, C. Fu, and H. Li, Shear-horizontal surface acoustic wave characteristics of a (110) ZnO/SiO₂/Si multilayer structure, *J. Alloys Comp.* **693**, 558 (2017).
- [43] Y. Ishii, R. Sasaki, Y. Nii, T. Ito, and Y. Onose, Magnetically Controlled Surface Acoustic Waves on Multiferroic BiFeO₃, *Phys. Rev. Appl.* **9**, 034034 (2018).
- [44] R. Verba, I. Lisenkov, I. Krivorotov, V. Tiberkevich, and A. Slavin, Nonreciprocal Surface Acoustic Waves in Multilayers With Magnetoelastic and Interfacial Dzyaloshinskii-Moriya Interactions, *Phys. Rev. Appl.* **9**, 064014 (2018).
- [45] K. Nakamura, Shear-Horizontal piezoelectric surface acoustic waves, *Jpn. J. Appl. Phys.* **46**, 4421 (2007).
- [46] R. Parmenter, The acousto-electric effect, *Phys. Rev.* **89**, 990 (1953).
- [47] A. R. Hutson and D. White, Elastic Wave propagation in piezoelectric semiconductors, *J. Appl. Phys.* **33**, 40 (1962).
- [48] C. Fu, K. Lee, K. Lee, and S. Yang, Low-intensity ultraviolet detection using a surface acoustic-wave sensor with a Ag-doped ZnO nanoparticle film, *Sm. Mat. Struct.* **24**, 015010 (2015).
- [49] P. Sharma and K. Sreenivas, Highly Sensitive ultraviolet detector based on ZnO/LiNbO₃ hybrid surface acoustic wave filter, *Appl. Phys. Lett.* **83**, 3617 (2003).
- [50] K. J. Lee, H. Oh, M. Jo, K. Lee, and S. Yang, An Ultraviolet sensor using spin-coated ZnO nanoparticles based on surface acoustic waves, *Microelectron. Eng.* **111**, 105 (2013).
- [51] Y. J. Guo, C. Zhao, X. S. Zhou, Y. Li, X. T. Zu, D. Gibson, and Y. Q. Fu, Ultraviolet sensing based on nanostructured ZnO/Si surface acoustic wave devices, *Sm. Mat. Struct.* **24**, 125015 (2015).
- [52] D. Royer and E. Dieulesaint, *Elastic Waves in Solids II* Translated by S. N. Lyle (Springer-Verlag, Heidelberg, 2000).
- [53] Steven G. Johnson, Shanhui Fan, Pierre R. Villeneuve, J. D. Joannopoulos, and L. A. Kolodziejski, Guided modes in photonic crystal slabs, *Phys. Rev. B* **60**, 5751 (1999).
- [54] M. Oudich, B. Djafari-Rouhani, B. Bonello, Y. Pennec, S. Hemaïdia, F. Sarry, and D. Beyssen, Rayleigh Waves in Phononic Crystal Made of Multilayered Pillars: Confined Modes, Fano Resonances, and Acoustically Induced Transparency, *Phys. Rev. Appl.* **9**, 034013 (2018).
- [55] M. Al Lethawe, M. Addouche, S. Benchabane, V. Laude, and A. Khelif, Guidance of surface elastic waves along a linear chain of pillars, *AIP Adv.* **6**, 121708 (2016).